Development of microfluidic flow cytometry capable of characterization of single-cell intrinsic structural and electrical parameters

OPEN ACCESS
IOP Publishing
Journal of Micromechanics and Microengineering
J. Micromech. Microeng. **32** (2022) 035007 (11pp)
https://doi.org/10.1088/1361-6439/ac5171

Development of microfluidic flow cytometry capable of characterization of single-cell intrinsic structural and electrical parameters

Hongyan Liang[1,2], Yi Zhang[1,2], Deyong Chen[1,2,3], Yueying Li[4], Yixiang Wang[5], Junbo Wang[1,2,3,*] and Jian Chen[1,2,3,*]

[1] State Key Laboratory of Transducer Technology (SKLTT), Aerospace Information Research Institute of Chinese Academy of Sciences (AIRCAS), Beijing, People's Republic of China
[2] School of Electronic, Electrical and Communication Engineering of University of Chinese Academy of Sciences (UCAS), Beijing, People's Republic of China
[3] School of Future Technology, University of Chinese Academy of Sciences (UCAS), Beijing, People's Republic of China
[4] Beijing Institute of Genomics of Chinese Academy of Sciences (BIGCAS), Beijing, People's Republic of China
[5] Peking University School of Stomatology (PUSS), Beijing, People's Republic of China

E-mail: chenjian@mail.ie.ac.cn and jbwang@mail.ie.ac.cn

Received 13 November 2021, revised 25 January 2022
Accepted for publication 2 February 2022
Published 14 February 2022

Abstract

Although single-cell intrinsic structural and electrical parameters (e.g. D_c of cell diameter, D_n of nuclear diameter, σ_{cy} of cytoplasmic conductivity and C_{sm} of specific membrane capacitance) are promising for cell-type classification, they cannot be obtained simultaneously due to structural limitations of previously reported flow cytometry. This paper presented a microfluidic flow cytometry made of a double T-type constriction channel plus a predefined fluorescence detection domain, capable of high-throughput characterizing single-cell D_c, D_n, σ_{cy} and C_{sm} leveraging a home-developed impedance-fluorescence model. As a demonstration, the microfluidic platform quantified D_c, D_n, σ_{cy} and C_{sm} from ~10 000 individual cells of three well-established tumor cell lines of A549, SW620 and HeLa where successful rates of cell-type classification were estimated as 54.5 ± 1.3% (D_c), 68.9 ± 6.8% ($D_c + D_n$) and 84.8 ± 4.4% (D_c, D_n, $\sigma_{cy} + C_{sm}$) based on neural pattern recognition. Then D_c, D_n, σ_{cy} and C_{sm} derived from ~10 000 single cells of K562 vs Jurkat of leukemia and SACC-LM vs CAL 27 of oral tumor were quantified and compared, where successful rates of cell-type classification were estimated as 87.3% (K562 vs Jurkat) and 79.5% (SACC-LM vs CAL 27), respectively. In summary, the microfluidic platform reported in this study could quantify single-cell intrinsic structural and electrical parameters simultaneously, leading to significant increases in successful rates of cell-type classification.

* Authors to whom any correspondence should be addressed.

Supplementary material for this article is available online

Keywords: flow cytometry, single-cell analysis, microfluidics, intrinsic structural and electrical parameters, high throughput

(Some figures may appear in colour only in the online journal)

1. Introduction

Single-cell intrinsic structural and electrical parameters including cell diameter (D_c), nuclear diameter (D_n), cytoplasmic conductivity (σ_{cy}) and specific membrane capacitance (C_{sm}) have been closely related to both physiological and pathological progresses of blood cells [1–4], tumor cells [5–8] and stem cells [9–12] due to cellular heterogeneity [13]. In particular, based on single-cell structural and/or electrical parameters, hematology analyzers have been well established for both three-part and five-part differentials of leukocytes [14]. However, previously reported methods for single-cell analysis cannot high-throughput obtain intrinsic structural and electrical parameters, which was introduced with comparison as follows.

As the golden approach of single-cell counting, initially the Coulter counter measured direct-current electric pulses of individual cells travelling through a small hole and calculated corresponding cell diameters of D_c, leading to the classification of leukocytes into mononuclear cells of lymphocytes and monocytes, and multinuclear cells of granulocytes [15–18]. With the inclusion of alternating-current components, the Coulter counter was capable of also measuring electrical properties of both membrane and cytoplasmic portions of single cells, to an extent, realizing the differential of leukocytes into mononuclear cells of lymphocytes and monocytes, and multinuclear cells of neutrophils, eosinophils and basophils [1, 19–21]. However, the Coulter counter cannot obtain the intrinsic structural marker of nuclei (D_n) and two intrinsic electrical markers of cytoplasmic conductivity (σ_{cy}) and specific membrane capacitance (C_{sm}) at the single-cell level, resulting in limited performances in cell-type classification.

In order to probe structural parameters of single nuclei, scattering flow cytometry was developed to capture multiple-angle scattered lights of a travelling single cell, where data of forward scattering was translated into D_c and data of side scattering indicated nuclear granularities [2, 5, 6, 22, 23]. Although this approach can to an extent measure nuclear structures of single cells, it still could not collect intrinsic structural and electrical parameters of single cells such as D_n, σ_{cy} and C_{sm}.

Aimed to measure intrinsic structural parameters of both D_c and D_n, imaging flow cytometry was developed to capture fluorescent images of travelling single cells with both membrane and nuclear portions stained [3, 4, 7, 24, 25]. Although this approach could report critical structural parameters of single cells based on further image processing, it cannot at the same time collect intrinsic electrical parameters of single cells and thus cannot provide comprehensive evaluations of individual cells.

Due to dimensional comparisons with biological cells, microfluidics was adopted to measure single-cell structural and electrical properties [8, 24]. More specifically, in microfluidic flow cytometry, single cells were flushed through detection regions where optical and electrical detections were realized [26–30], and the measured optical/electrical parameters were used for cell-type classification. However, in these previously developed microfluidic platforms, inherent structural markers such as nuclear diameter (D_n) and electrical markers such as cytoplasmic conductivity (σ_{cy}) and specific membrane capacitance (C_{sm}) cannot be quantified due to limitations in detection structures and lacks of equivalent optical/electrical models.

To address this issue, this paper presented a microfluidic flow cytometry made of a double T-type constriction channel (cross-sectional area smaller than a cell) with a predefined fluorescence detection domain, enabling high-throughput measurements of single-cell D_c, D_n, σ_{cy} and C_{sm}. More specifically, when single cells with fluorescence stained nuclei deformed through and properly filled the constriction channel, D_c, σ_{cy} and C_{sm} were derived from impedance signals while D_n was derived from fluorescence signals leveraging a home-developed impedance-fluorescence model for the constriction channel.

In comparison to Coulter counters, scattering, imaging flow cytometry and previously reported microfluidic optical/electrical flow cytometry, the microfluidic platform reported in this paper could measure intrinsic structural and electrical parameters of single cells in a high-throughput manner, providing a more comprehensive evaluation of single cells.

2. Methodology

2.1. Material purchase

Cell types containing three well-established carcinoma cell lines of A549 (lung), SW620 (colon) and HeLa (cervix), leukemia cell lines of K562 (chronic myeloid tumor) and Jurkat (acute T-cell tumor), and oral carcinoma cell types of SACC-LM (salivary) and CAL 27 (tongue) were bought from the National Experimental Cell Resource Sharing Service Platform (China).

Unless otherwise indicated, reagents for cell culture were bought from Life Technologies (USA). Fluorochrome Hoechst 33342 used for nuclear staining was bought from Sigma Aldrich (USA). Materials for the fabrication of microfluidic flow cytometry including photoresist of AZ serial, 184 silicone elastomer and SU 8-25 negative photoresist were purchased from AZ Electronic Materials (USA), Dow Corning (USA) and MicroChem (USA), respectively.

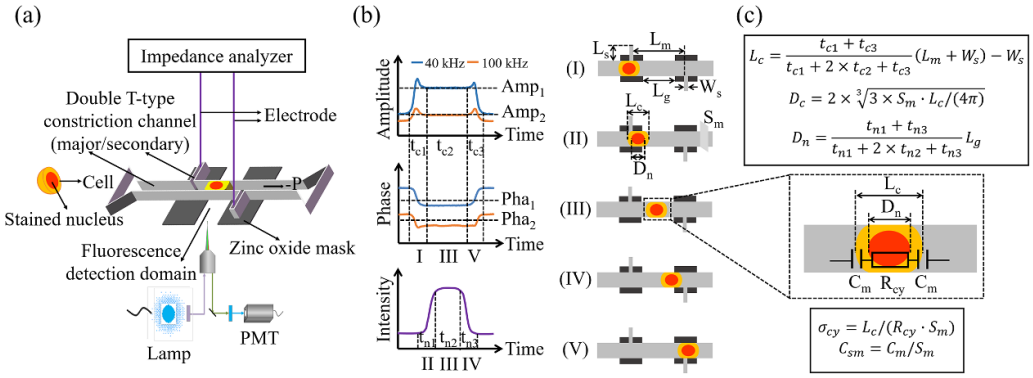

Figure 1. (a) Schematic of the microfluidic flow cytometry made of a double T-type constriction channel plus a predefined fluorescence detection domain, where a traveling cell with a fluorescence stained nucleus was squeezed through the constriction channel with varied electrical and optical signals detected by an impedance analyzer and a photomultiplier tube, respectively. (b) Preliminary electrical and optical signals of the traveling cell were divided into five domains (I–V) leveraging the impedance-fluorescence model for the constriction channel. (c) Corresponding time durations of t_{c1}, t_{c2} and t_{c3} from three domains of impedance (I, III and V) were obtained and translated into cell diameter of D_c while time durations of t_{n1}, t_{n2} and t_{n3} from three domains of fluorescence (II–IV) were acquired and translated into nuclear diameter of D_n. Furthermore, impedance values ($Amp_1 + Pha_1$ and $Amp_2 + Pha_2$) from domain III of impedance were quantified and translated into cytoplasmic conductivity of σ_{cy} and specific membrane of C_{sm}.

2.2. Cell preparation

All cells were cultured under the conditions of 37 °C and 5% CO_2. To be more specific, RPMI-1640 medium (10% foetal bovine serum, 1% penicillin and 1% streptomycin) was used to culture A549, SW620, SACC-LM, K562 and Jurkat cells. Meanwhile, DMEM medium (10% foetal bovine serum, 1% penicillin and 1% streptomycin) was used to culture HeLa and CAL 27 cells. For nuclear staining, living cells were collected by centrifugation and added with 10% fluorochrome Hoechst 33342 for an incubation of 5 min at 37 °C. After incubation, cells were washed for three times and collected by centrifugation at 4 °C, and then resuspended in phosphate buffer saline (PBS) containing 0.5% bovine serum albumin.

2.3. Working mechanism

Figure 1 shows the working mechanism of the microfluidic flow cytometry which was made of a double T-type constriction channel plus a predefined fluorescence detection domain and was capable of high-throughput measuring intrinsic structural (D_c of cell diameter and D_n of nuclear diameter) and electrical (σ_{cy} of cytoplasmic conductivity and C_{sm} of specific membrane capacitance) parameters for individual cells. More specifically, when a cell with a fluorescence stained nucleus deformed through and properly filled the constriction channel, D_c, σ_{cy} and C_{sm} were derived from impedance signals while D_n was derived from fluorescence signals leveraging a home-developed impedance-fluorescence model for the constriction channel.

Figure 1(a) shows major components of the microfluidic flow cytometry for single-cell analysis including the aforementioned double T-type constriction channel for cell travelling, an impedance analyzer for electrical property measurements and a photomultiplier tube for optical property measurements. As to the double T-type constriction channel, it mainly included a major constriction channel for cell squeezing, two secondary constriction channels for electrical acquisition, and a fluorescence detection domain formed by a patterned zinc oxide window for fluorescent detection. In operation, a travelling cell with a fluorescence stained nucleus was squeezed through the major constriction channel where varied electrical and optical signals were detected by the impedance analyzer and the photomultiplier tube, simultaneously.

Preliminary electrical and optical signals of the travelling cell were divided into five domains (I–V) based on the impedance-fluorescence model for the constriction channel composed of five key geometrical parameters: cross sectional area (S_m) and length (L_m) of the major constriction channel, width of the secondary constriction channels (W_s), gap of the fluorescence detection domain (L_g) and cell elongation length (L_c) (see figure 1(b)). More specifically, for each impedance pulse, it was segmented into three time durations (e.g. cell entering (I), passing (III) and leaving (V)). For domain I and V, time durations of t_{c1} and t_{c3} with the same corresponding travelling distance of $W_s + L_c$ were obtained. As to domain III, a time duration of t_{c2} with a corresponding travelling distance of $L_m - L_c$ was obtained and corresponding electrical parameters of $Amp_1 + Pha_1$ and $Amp_2 + Pha_2$ were also acquired.

Meanwhile, for each fluorescence pulse, it was divided into three time durations (e.g. nuclear entering (II), passing (III) and leaving (IV)). For domain II and IV, time durations of t_{n1} and t_{n3} with the same corresponding travelling distance of D_n were obtained, and for domain III, time duration of t_{n2} with a corresponding travelling distance of L_g-D_n was acquired.

Figure 1(c) shows the translation of raw time and impedance data into single-cell intrinsic structural and electrical parameters of D_c, D_n, C_{sm} and σ_{cy}. As to the quantification of D_c, L_c was first calculated under the assumptions of (a) a steady velocity for a travelling cell and (b) $L_m > L_c$. More specifically, for domain I, III and V with time durations of t_{c1}, t_{c2} and t_{c3}, the corresponding travelling distances were

$W_s + L_c$, $L_m - L_c$ and $W_s + L_c$, respectively. Thus, L_c was obtained as follows:

$$\frac{(W_s+L_c)+2\times(L_m-L_c)+(W_s+L_c)}{t_{c1}+2\times t_{c2}+t_{c3}} = \frac{(W_s+L_c)+(W_s+L_c)}{t_{c1}+t_{c3}} \quad (1a)$$

$$L_c = \frac{t_{c1}+t_{c3}}{t_{c1}+2\times t_{c2}+t_{c3}}(L_m+W_s)-W_s. \quad (1b)$$

Then under the assumption that a cell was incompressible, the volume of the deformed cell in the constriction channel which was treated as a cuboid with an length of L_c and an cross-sectional area of S_m was equal with the volume of the cell in sphere with a diameter of D_c. Thus, D_c was obtained as follows:

$$D_c = 2\times\sqrt[3]{3\times S_m\cdot L_c/(4\pi)}. \quad (2)$$

As to the quantification of D_n, it was measured under the assumptions of (a) a steady velocity for a travelling cell and (b) $L_g > D_n$. More specifically, for domain II, III and IV with time durations of t_{n1}, t_{n2} and t_{n3}, the corresponding travelling distances were D_n, L_g-D_n and D_n, respectively. Thus, D_n was obtained as follows:

$$D_n = \frac{t_{n1}+t_{n3}}{t_{n1}+2\times t_{n2}+t_{n3}}L_g. \quad (3)$$

As to the quantification of σ_{cy} and C_{sm}, figure 1(c) shows key electrical components of a travelling cell within the major constriction channel including R_{cy} of cytoplasmic resistance and C_m of membrane capacitance which were obtained by electrical parameters of $Amp_1 + Pha_1$ and $Amp_2 + Pha_2$ for the travelling cell. R_{cy} and C_m as intermediate electrical parameters were further processed to σ_{cy} and C_{sm} when geometrical dimensions of the constriction channel were taken into consideration:

$$\sigma_{cy} = L_c/(R_{cy}\cdot S_m) \quad (4)$$

$$C_{sm} = C_m/S_m. \quad (5)$$

2.4. Device design and fabrication

For the microfluidic flow cytometry to function properly, key geometric parameters of the double T-type constriction channel including the major constriction channel's cross sectional area (S_m) and length (L_m), fluorescence detection domain's gap (L_g) and the secondary constriction channels' cross sectional area (S_s) were designed carefully, as follows.

The major constriction channel's cross sectional area (S_m) has to be slightly smaller than the cross sectional area of the cell under measurement to ensure proper deformation of the cell to effectively block electric lines without damages for cell membrane and nuclear portions. When the diameters of the cells under measurement were estimated as ~15 μm, S_m of 10 μm × 10 μm was chosen in this study.

As to the choice of the major constriction channel's length (L_m), if L_m was too long, it could increase both basal impedance values without cells and cellular travelling durations, leading to compromised measurement sensitivities and throughputs. If L_m was too short, it could not meet the requirement of the impedance-fluorescence model, resulting in inaccurate measurements of intrinsic single-cell structural parameters. When these two factors were taken into consideration, L_m was set as 50 μm in this study. Similarly, since L_g cannot be too large or too small in this study, it was set as 25 μm under the consideration of ~10 μm of D_n and 10 μm × 10 μm of S_m. Note that the fluorescence detection domain was formed by patterned zinc oxide which was used to block the excitation light of 355 nm for Hoechst 33342 in nuclear staining.

Considering that the secondary constriction channels' height was the same as that of the major constriction channel, the secondary constriction channels' cross sectional area (S_s) was mainly determined by its width. S_s should be as small as possible so that travelling single cells can effectively seal without entering the secondary constriction channels. Meanwhile, the increase in S_s can decrease the impedance values of the constriction channels without cells. In addition, when resolutions of microfabrication were also considered, S_s was defined as 3 μm × 10 μm in this paper.

The device fabrication consisted of three key steps, which were the fabrications of the double T-type constriction channel, the fluorescence detection domain and the bonding of these two components (see figure S1 (available online at stacks.iop.org/JMM/32/035007/mmedia)). More specifically, the microfabrication of the double T-type constriction channel included key steps of (a) exposure of AZ 5214, (b) development of AZ 5214, (c) deep reactive ion etching of silicon, (d) exposure of SU 8-25, (e) development of SU 8-25, (f) molding of Polydimethylsiloxane (PDMS), and (g) peeling of PDMS (see figure S1(a)).

Next, fabrication of the fluorescence detection domain included key steps of (a) exposure of AZ 1500, (b) development of AZ 1500, (c) sputtering of zinc oxide, (d) lift-off of zinc oxide, and (e) coating of PDMS (see figure S1(b)). Figure S1(c) shows the bonding of the fabricated of double T-type constriction channel plus the predefined fluorescence detection domain enabled by an oxygen plasma treatment and figure S1(d) shows a fabricated microfluidic device with the double T-type constriction channel and the fluorescence detection domain highlighted.

2.5. Device operation

In operation, the microfabricated platform was first filled with PBS and the corresponding fluorescence detection domain was photobleached by a fluorescence microscope (IX73, Olympus, Japan). Then suspended cells stained with Hoechst 33342 (20 ~ 50 μl, ~5 × 10^6 cells ml^{-1}) were aspirated through the constriction channel under a negative pressure of ~2 kPa (DPI-610, Druck, UK).

An impedance analyzer (MFLI 5 M, Zurich Instruments, CH) based on 40 and 100 kHz sinusoidal signals

(root-mean-square voltage of 0.5 V, time constant of 25 μs) were connected with two secondary constriction channels using silver wires to measure impedance data of squeezing individual cells. Meanwhile, when the stained nuclei in single cells traveled through the fluorescence detection domain, it was excited with a metal halide lamp (X-Cite 120Q, Excelitas, Canada) at a 100% output power with a bandpass filter (AT375/28x, Chroma, USA). A photomultiplier tube of H10723-20 (Hamamatsu, Japan) plus a bandpass filter of AT460/50 m (Chroma, USA) was used for fluorescent detection. The impedance profiles and fluorescence signals were further collected by a data acquisition card of USB-6349 (NI, USA) under a sampling rate of 100 kHz. Note that the inclusion of 40 and 100 kHz sinusoidal signals were based on a previous study where frequencies of single-cell impedance measurements were finely tuned [31].

2.6. Data analysis

Raw impedance profiles were translated into intrinsic structural and electrical parameters (e.g. D_c of cell diameter, σ_{cy} of cytoplasmic conductivity and C_{sm} of specific membrane capacitance) based on the following two parts. First, D_c was quantified leveraging two steps: (a) kernel-based density estimation of preliminary impedance profiles at 100 kHz with binarization to locate individual pulses representing travelling single cells; (b) kernel-based density estimation and binarization to divide individual pulses into three domains of entering (t_{c1}), travelling (t_{c2}) and leaving (t_{c3}) the double T-type constriction channel, enabling the calculation of D_c (see figure 1(c) and equations (1*a*), (1*b*), (2)). Note that since peaks and valleys of preliminary impedance profiles at 100 kHz were more obvious than the counterparts at 40 kHz, 100 kHz impedance data were used in the calculation of D_c.

After the quantification of D_c, raw impedance profiles were further translated into σ_{cy} and C_{sm} leveraging four steps. (a) Weighted averages of the raw impedance profiles in the traveling domain within the double T-type constriction channel were processed into two-frequency amplitude values of $Amp_1 + Amp_2$ and phase values of $Pha_1 + Pha_2$. (b) Preliminary impedance parameters of Amp_1, Amp_2, Pha_1 and Pha_2 were translated into the equivalent impedance of the travelling cell at both 40 and 100 kHz, based on equivalent electrical components of the empty constriction channel (see figure 1(c)). (c) The equivalent impedance of the travelling cell was further decoupled into cytoplasmic resistance of R_{cy} and membrane capacitance of C_m which were in series. (d) Based on equation (4) and (5)), when geometric parameters of the constriction channel were taken into consideration, R_{cy} and C_m were translated into σ_{cy} and C_{sm}.

Raw fluorescence profiles were translated into the intrinsic structural parameter (nuclear diameter of D_n) based on three steps: (a) median filtration of preliminary fluorescence profiles to obtain valid signals; (b) kernel-based density estimation and binarization of filtered signals to locate individual pulses representing traveling single nuclei of corresponding cells; and (c) curve fitting based on the least-square principle to divide individual pulses into three domains of entering (t_{n1}), travelling (t_{n2}) and leaving (t_{n3}) the fluorescence detection region, enabling the quantification of D_n (see figure 1(c) and equation (3)).

2.7. Statistical analysis

Multiple samples were measured and the results were expressed as mean $\pm$ standard deviation. In order to determine the level of differences, the student's *t*-test was conducted where P value < 0.05 (*) was considered with statistically significant difference.

In addition, pattern recognition enabled by two-layer forward-feedback neural network (MATLAB 2016b, MathWorks, USA) was used to predict successful rates of cell-type classification. In this study, the results of two cell types with quantified single-cell values of D_c, D_n, σ_{cy} and C_{sm} were used as inputting matrix, which was divided into 70% for training, 15% for validation and 15% for testing. Note that for all the inputting data points, values of single-cell D_c, D_n, σ_{cy} and C_{sm} and specific cell types were clear. After training of 70% data and validation of 15% data, a 'code function' was generated to map single-cell values of D_c, D_n, σ_{cy} and C_{sm} with specific cell types. Then the obtained 'code function' was used to process 15% data points for testing and the results of cell types generated from the 'code function' were compared with the true cell types, producing a 'successful rate' as an indicator to determine the accuracy of cell-type classification. For an incoming cell with quantified D_c, D_n, σ_{cy} and C_{sm}, these values were applied into the code function and the generated value of '0' or '1' indicated the specific cell type.

3. Results and discussion

Constriction channels have been developed to measure electrical properties of individual cells where squeezing cells blocked electric lines dramatically, and the corresponding impedance variations were translated into intrinsic electrical parameters based on an equivalent electrical model. Developments of constriction channels witnessed structural improvements from straight [32] to crossing [33] and then double T-type [31] constriction channels, capable of quantifying single-cell structural and electrical parameters of D_c, σ_{cy} and C_{sm} in a high-throughput manner. Based on D_c, σ_{cy} and C_{sm}, classifications of tumor cells with different malignant levels [32], stem cells with variously differentiation capabilities [34] and sub-group white blood cells [35] were demonstrated. However, previously reported constriction channels cannot measure biophysical properties of nuclear portions and thus cannot provide a comprehensive evaluation of biological cells.

3.1. Platform characterization

This study developed the microfluidic flow cytometry which was made of the double T-type constriction channel plus the predefined fluorescence detection domain and was capable

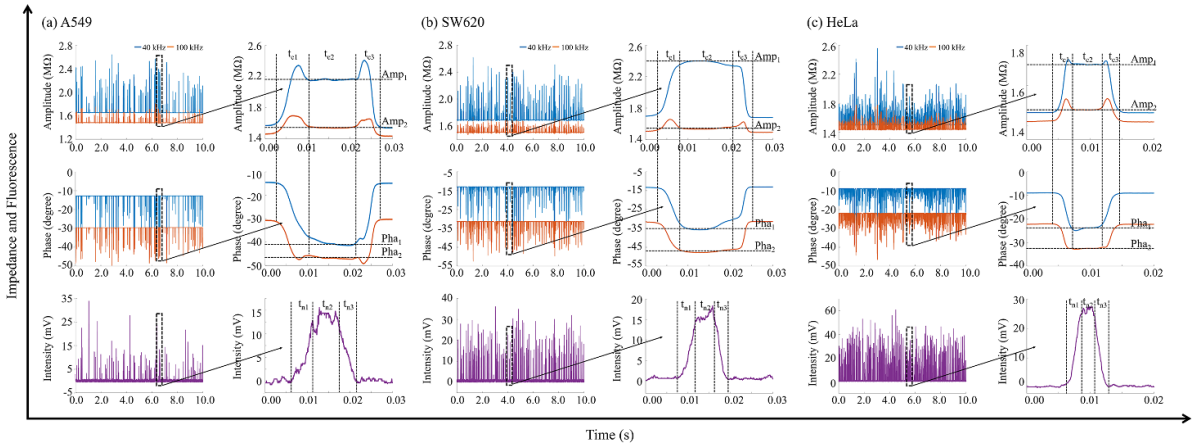

Figure 2. Raw impedance profiles at 40 and 100 kHz, and fluorescence data @355 nm for excitation and @465 nm for detection of individual A549 (a), SW620 (b) and HeLa (c) cells. Electrical peaks in amplitude, valleys in phase and fluorescence peaks in intensity indicate events of cell travelling in the double T-type constriction channel plus the predefined fluorescence detection domain. For each cell, impedance and fluorescence variations were processed to duration parameters t_{c1}, t_{c2} and t_{c3} of impedance, t_{n1}, t_{n2} and t_{n3} of fluorescence as well as electrical impedance values of $Amp_1 + Pha_1$ and $Amp_2 + Pha_2$.

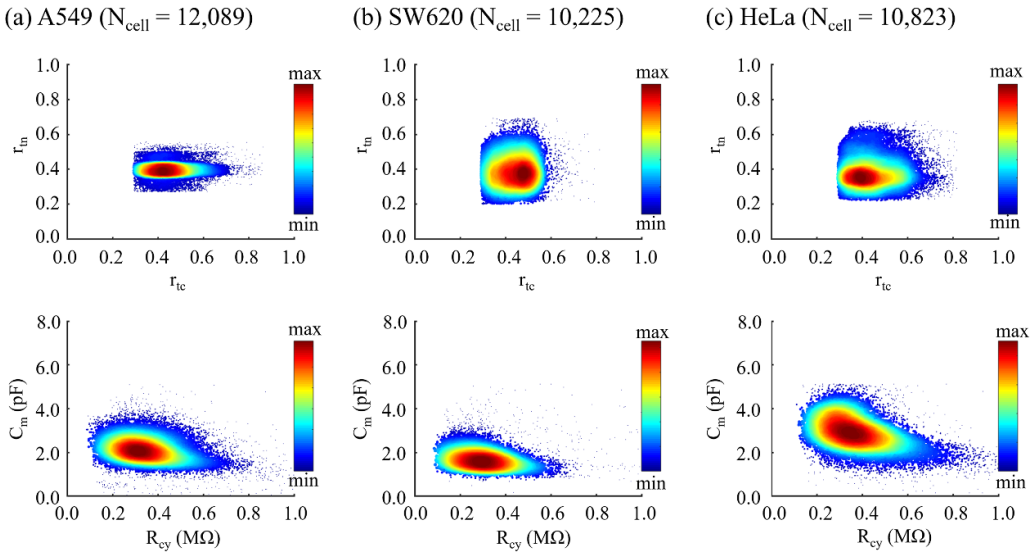

Figure 3. Scatter plots of four vital intermediate indicators containing structural parameters of $r_{tc} + r_{tn}$, and electrical parameters of $R_{cy} + C_m$ for three well-established carcinoma cell lines of A549 (a, $N_{cell} = 12\,089$), SW620 (b, $N_{cell} = 10\,225$) and HeLa (c, $N_{cell} = 10\,823$).

of high-throughput measurements of intrinsic structural and electrical parameters of D_c, D_n, σ_{cy} and C_{sm} for individual cells leveraging the home-developed impedance-fluorescence model. In the stage of platform characterization, figure 2 shows raw impedance profiles at 40 and 100 kHz, and fluorescence data with excitation at 355 nm and detection at 465 nm of individual A549 (a), SW620 (b) and HeLa (c) cells. Here electrical peaks in amplitude, valleys in phase and fluorescence peaks in intensity indicate a cell travelling in the double T-type constriction channel plus the predefined fluorescence detection domain.

For each cell, impedance and fluorescence variations were processed to time duration parameters t_{c1}, t_{c2} and t_{c3} of impedance, t_{n1}, t_{n2} and t_{n3} of fluorescence as well as electrical impedance values of $Amp_1 + Pha_1$ and $Amp_2 + Pha_2$. These results indicated the microfluidic system reported in this paper can (a) capture preliminary impedance and fluorescent signals of squeezing individual cells simultaneously; (b) extract key time and impedance parameters based on impedance and fluorescence pulses.

Figure 3 shows scatter plots of four vital intermediate parameters containing structural indicators of r_{tc} $((t_{c1} + t_{c2})/(t_{c1} + 2 \times t_{c2} + t_{c3}))$, r_{tn} $((t_{n1} + t_{n2})/(t_{n1} + 2 \times t_{n2} + t_{n3}))$, and electrical indicators of C_m, R_{cy} for three well-established carcinoma cell lines of A549 (a, $N_{cell} = 12\,089$), SW620 (b, $N_{cell} = 10\,225$) and HeLa (c, $N_{cell} = 10\,823$). More specifically, as indicators of D_c and D_n, r_{tc} and r_{tn} were quantified as 0.46 ± 0.10 and 0.40 ± 0.04 for A549, 0.44 ± 0.08 and 0.40 ± 0.09 for SW620, 0.46 ± 0.10 and 0.39 ± 0.09 for HeLa cells, respectively. These

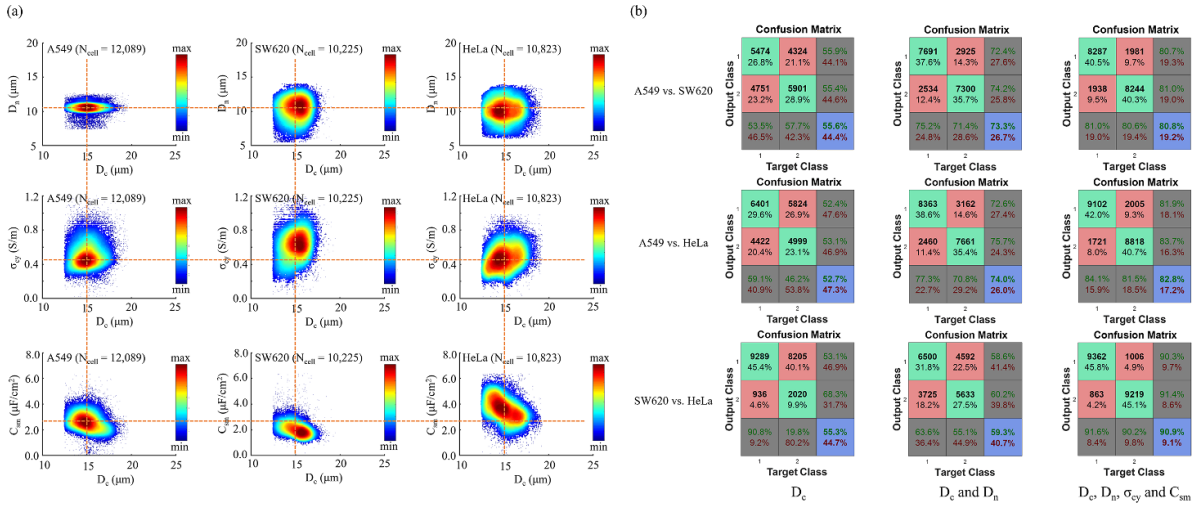

Figure 4. (a) Scatter plots of four intrinsic structural and electrical parameters of single cells including D_c vs D_n, D_c vs σ_{cy} and D_c vs C_{sm} for A549 ($N_{cell} = 12\,089$), SW620 ($N_{cell} = 10\,225$) and HeLa ($N_{cell} = 10\,823$). (b) Confusion matrixes of A549 vs SW620, A549 vs HeLa, and SW620 vs HeLa cells under the input parameters of D_c only, $D_c + D_n$, and D_c, D_n, σ_{cy} and C_{sm} together. Note that the numbers in the bottom right-hand boxes of the matrixes indicated successful rates of cell-type classification.

results indicated that these three cell types had comparable geometrical structures in term of cell and nuclear diameters.

Meanwhile, as indicators of σ_{cy} and C_{sm}, R_{cy} and C_m were calculated as 0.38 ± 0.28 MΩ and 2.13 ± 0.63 pF for A549, 0.32 ± 0.22 MΩ and 1.72 ± 0.51 pF for SW620, 0.40 ± 0.26 MΩ and 2.85 ± 0.81 pF for HeLa cells. Significant differences of R_{cy} and C_m among A549, SW620 and HeLa cells were found, indicating that cells with similar geometrical parameters may be differentiated based on electrical properties.

Figure 4(a) shows scatter plots of four intrinsic structural and electrical parameters including D_c vs D_n, D_c vs σ_{cy} and D_c vs C_{sm} for A549 ($N_{cell} = 12\,089$), SW620 ($N_{cell} = 10\,225$) and HeLa ($N_{cell} = 10\,823$), respectively. More specifically, structural parameters including D_c and D_n were quantified as 15.2 ± 1.4 μm and 10.5 ± 0.8 μm for A549 cells, 15.0 ± 1.2 μm and 10.2 ± 1.7 μm for SW620 cells, 15.1 ± 1.4 μm and 10.1 ± 1.7 μm for HeLa cells. For these three cell lines, comparable results of D_c and D_n were also derived from microscopic images, which were 15.2 ± 1.3 μm and 10.2 ± 1.6 μm for A549, 14.9 ± 1.6 μm and 10.0 ± 1.6 μm for SW620, 15.1 ± 1.9 μm and 9.9 ± 1.6 μm for HeLa. These results proved that the developed microfluidic system can obtain D_c and D_n from large populations of single cells with high accuracies.

Meanwhile, electrical parameters including σ_{cy} and C_{sm} were calculated as 0.53 ± 0.17 S m^{-1} and 2.64 ± 0.78 μF cm^{-2} for A549 cells, 0.62 ± 0.19 S m^{-1} and 2.13 ± 0.63 μF cm^{-2} for SW620 cells, 0.49 ± 0.16 S m^{-1} and 3.54 ± 1.00 μF cm^{-2} for HeLa cells. These results fell within the ranges of σ_{cy} (∼1 S m^{-1}) and C_{sm} (∼1 μF cm^{-2}) obtained by conventional tools such as electrorotation and patch clamping with limited throughputs [36]. Comparable results of σ_{cy} and C_{sm} were also derived from the double T-type constriction channel without the fluorescence detection domain, which were 0.49 ± 0.07 S m^{-1} and 2.46 ± 0.55 μF cm^{-2} for A549, 0.52 ± 0.07 S m^{-1} and 2.00 ± 0.51 μF cm^{-2} for SW620, 0.51 ± 0.07 S m^{-1} and 3.28 ± 0.65 μF cm^{-2} for HeLa cells [31]. These results indicated that the step of nuclear staining had negligible effects on intrinsic electrical parameters of single cells. In addition, there were significant differences of σ_{cy} and C_{sm} among A549, SW620 and HeLa cells, indicating that single cells with similar structural parameters may be differentiated based on electrical parameters.

Figure 4(b) shows confusion matrixes of A549 vs SW620, A549 vs HeLa, and SW620 vs HeLa under the input parameters of D_c only, $D_c + D_n$, D_c, D_n, σ_{cy} and C_{sm} together where the numbers in the bottom right-hand boxes of the matrixes indicated successful rates of cell-type classification.

Based on D_c only, the successful rates of classifying carcinoma cell lines were estimated as 55.6% (A549 vs SW620), 52.7% (A549 vs HeLa) and 55.3% (SW620 vs HeLa), suggesting limited results of cell-type classification when only D_c was used. Then based on D_c and D_n, the successful rates of cell-type classification were increased to 73.7% (A549 vs SW620), 74.0% (A549 vs HeLa) and 59.3% (SW620 vs HeLa), revealing that D_n could contribute to cell-type classification to an extent.

Furthermore, when D_c, D_n, σ_{cy} and C_{sm} were used in combination, the successful rates of cell-type classification were further improved to 80.8% (A549 vs SW620), 82.8% (A549 vs HeLa) and 90.9% (SW620 vs HeLa). These results indicated that the combination of intrinsic structural and electrical parameters of D_c, D_n, σ_{cy}, and C_{sm} can be used to effectively estimate cellular status. In addition, the successful rates of cell-type classification based on D_c, D_n, σ_{cy} and C_{sm} were significantly higher than the counterparts based on D_c, σ_{cy} and C_{sm}, which were 75.6% (A549 vs SW620), 77.2% (A549 vs HeLa) and 90.4% (SW620 vs HeLa), indicating that the inclusion of the fluorescence detection region within the double T-type constriction channel could effectively contribute to cell-type classification.

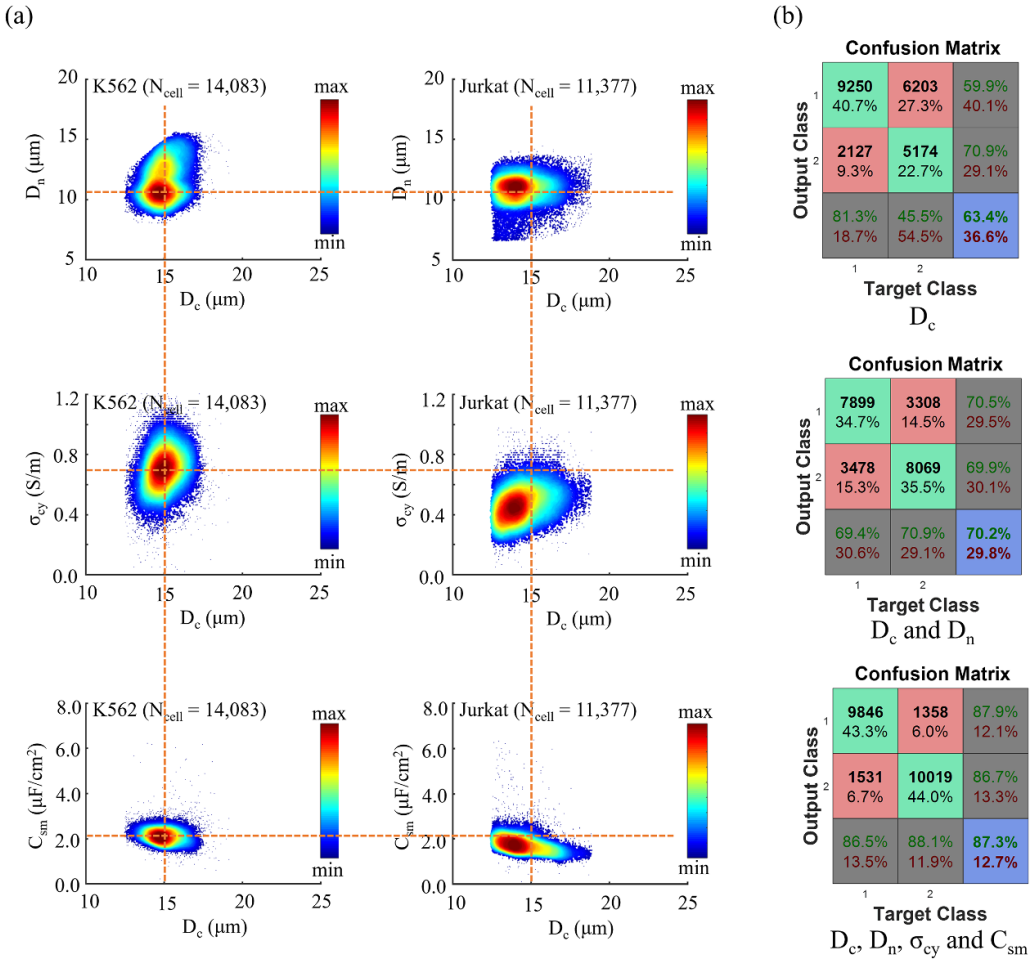

Figure 5. (a) Scatter plots of four intrinsic structural and electrical parameters of single cells including D_c vs D_n, D_c vs σ_{cy} and D_c vs C_{sm} for leukemia cell lines of K562 (N_{cell} = 14 083) and Jurkat (N_{cell} = 11 377). (b) Confusion matrixes of K562 vs Jurkat cells under D_c only, $D_c + D_n$, and D_c, D_n, σ_{cy} and C_{sm} together. Note that the numbers in the bottom right-hand boxes of the matrixes indicated successful rates of cell-type classification.

3.2. Platform demonstration

As a demonstration, the microfluidic system in this paper was first used to classify leukemia cell lines of K562 and Jurkat. Preliminary electrical and optical profiles, and processed data of r_{tc}, r_{tn}, R_{cy} and C_m for K562 and Jurkat cells were shown in figures S2 and S3. Final results of intrinsic structural and electrical parameters of D_c, D_n, σ_{cy} and C_{sm} of K562 (N_{cell} = 14 083) vs Jurkat (N_{cell} = 11 377) were shown in figure 5(a), which were 15.0 ± 1.0 vs 14.7 ± 1.4 μm, 11.6 ± 1.6 vs 10.7 ± 1.3 μm, 0.70 ± 0.15 vs 0.48 ± 0.13 S m^{-1} and 2.12 ± 0.34 vs 1.78 ± 0.44 μF cm^{-2}, respectively. These results indicated that single cells with comparable structural parameters (D_c and D_n) may be differentiated based on variations in electrical parameters (σ_{cy} and C_{sm}).

Figure 5(b) shows confusion matrixes of K562 vs Jurkat cells under the input parameters of D_c only, $D_c + D_n$, D_c, D_n, σ_{cy} and C_{sm} in combination where the numbers in the bottom right-hand boxes of the matrixes indicated successful rates of classifying cell types. The successful rates of cell-type classification of K562 vs Jurkat were estimated as 63.4% (D_c), 70.2% (D_c and D_n) and 87.3% (D_c, D_n, σ_{cy} and C_{sm}). These results of cell-type classification were due to the fact that these two leukemia cell lines demonstrated comparable structural parameters of D_c and D_n with less than 10% differences and significant differences in σ_{cy} with a ~40% difference and C_{sm} with a ~20% difference. Thus the combination of intrinsic structural and electrical parameters of single cells including D_c, D_n, σ_{cy} and C_{sm} can be used to effectively classify leukemia cell lines of K562 and Jurkat.

Similarly, oral carcinoma cell lines of SACC-LM and CAL 27 were characterized and compared in this study, where corresponding raw and intermediate data were also shown in figures S2 and S3. The final results of intrinsic structural and electrical parameters of D_c, D_n, σ_{cy} and C_{sm} of SACC-LM (N_{cell} = 13 326) vs CAL 27 (N_{cell} = 11 218) were shown in figure 6(a), which were 15.7 ± 1.4 vs 14.5 ± 1.2 μm, 10.4 ± 1.4 vs 9.2 ± 1.3 μm, 0.51 ± 0.13 vs 0.58 ± 0.13 S m^{-1} and 2.73 ± 0.69 vs 2.80 ± 0.63 μF cm^{-2}, respectively.

The successful rates of cell-type classification of SACC-LM vs CAL 27 were shown in figure 6(b), which were estimated as 67.8% (D_c), 73.7% (D_c and D_n) and 79.5% (D_c, D_n, σ_{cy} and C_{sm}). Different from leukemia cell lines of K562 and Jurkat, these two oral carcinoma cell lines demonstrated

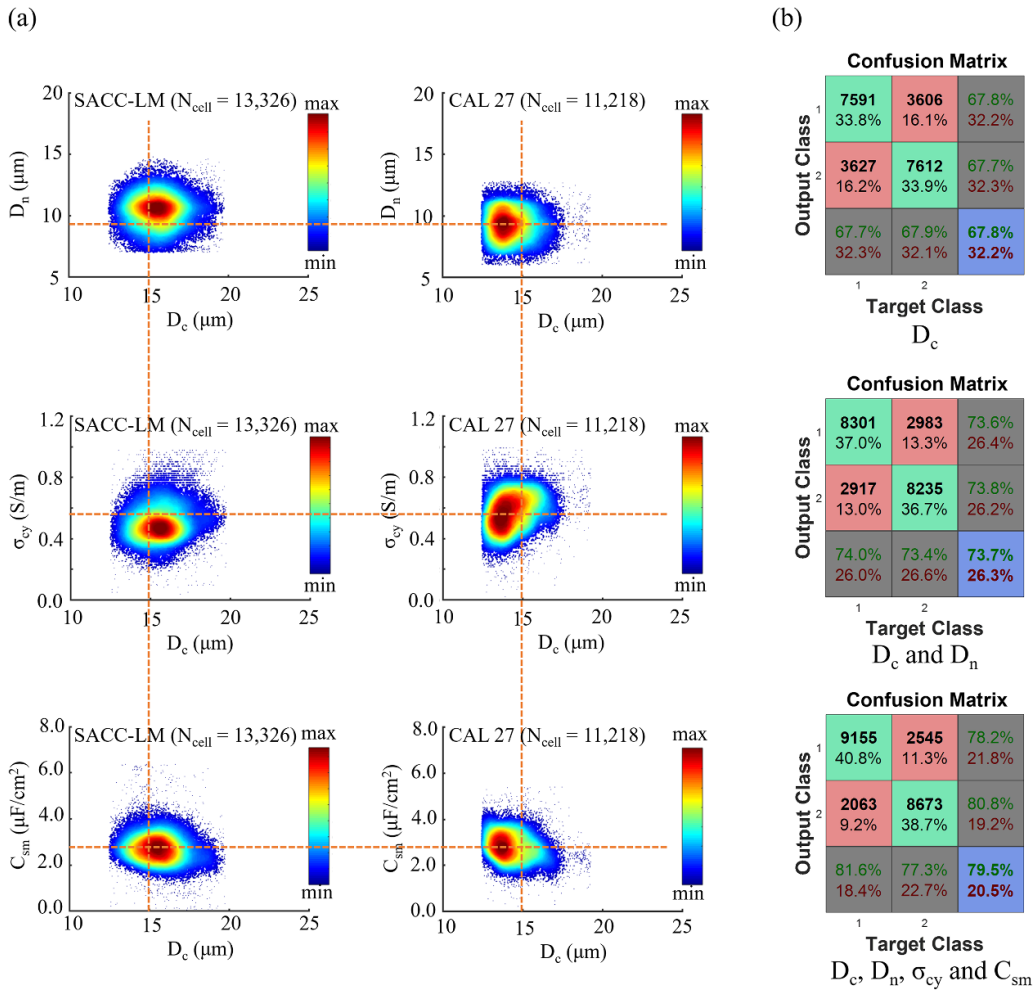

Figure 6. (a) Scatter plots of four intrinsic structural and electrical parameters including D_c vs D_n, D_c vs σ_{cy} and D_c vs C_{sm} for oral carcinoma cell lines of SACC-LM (N_{cell} = 13 326) and CAL 27 (N_{cell} = 11 218). (b) Confusion matrixes of SACC-LM vs CAL 27 cells under D_c only, $D_c + D_n$, and D_c, D_n, σ_{cy} and C_{sm} together. Note that the numbers in the bottom right-hand boxes of the matrixes indicated successful rates of cell-type classification.

limited differences (∼10%) in both structural and electrical parameters. However, the combination of intrinsic structural and electrical parameters of single cells including D_c, D_n, σ_{cy} and C_{sm} can improve the successful rates of differentiating SACC-LM from CAL 27.

Furthermore, for the comparisons of K562 vs Jurkat cells and SACC-LM vs CAL 27 cells, the inclusion of the intrinsic structural parameter of D_n contributed to the increases of the classification rate from 85.1% (K562 vs Jurkat) and 74.0% (SACC-LM vs CAL 27) based on D_c, σ_{cy} and C_{sm} derived from the previously reported double T-type constriction channel [31] to 87.3% (K562 vs Jurkat) and 79.5% (SACC-LM vs CAL 27) based on D_c, D_n, σ_{cy} and C_{sm} derived from the double T-type constriction channel plus the predefined fluorescence detection domain reported in this study. Note that since K562 vs Jurkat and SACC-LM vs CAL 27 have comparable structural parameters of cell and nuclear diameters, the inclusion of D_n was observed to demonstrate a limited effect on cell-type classification. If two cell lines with significant differences in geometrical parameters were compared, the intrinsic structural parameter of D_n may function as an enabling parameter in cell-type classification.

4. Conclusions

In summary, this paper presented the microfluidic flow cytometry made of the double T-type constriction channel plus the predefined fluorescence detection domain, capable of high-throughput measurements of single-cell intrinsic structural parameters of cell diameter (D_c) and nuclear diameter (D_n), and electrical markers of cytoplasmic conductivity (σ_{cy}) and specific membrane capacitance (C_{sm}). As to platform characterization, this microfluidic flow cytometry was demonstrated to quantify D_c, D_n, σ_{cy} and C_{sm} from three well-established carcinoma cell lines with high accuracies. As for platform demonstration, D_c, D_n, σ_{cy} and C_{sm} from leukemia and oral tumors were measured, demonstrating higher successful rates of cell-type classification when these four parameters were used compared to the results using individual biophysical markers only.

Data availability statement

All data that support the findings of this study are included within the article (and any supplementary files).

Acknowledgments

The authors acknowledge financial supports from the NSFC (Nos. 61825107, 61922079 and 62121003), YIPA (Y201927), Instrument Research and Development (GJJSTD20210004), and Key Project (QYZDB-SSW-JSC011) of Chinese Academy of Sciences (CAS).

Conflict of interest

The authors declare no conflicts of interest.

ORCID iD

Jian Chen https://orcid.org/0000-0003-4612-3279

References

[1] Simon P, Frankowski M, Bock N and Neukammer J 2016 Label-free whole blood cell differentiation based on multiple frequency AC impedance and light scattering analysis in a micro flow cytometer *Lab Chip* **16** 2326–38
[2] Dannhauser D, Rossi D, Ripaldi M, Netti P A and Causa F 2017 Single-cell screening of multiple biophysical properties in leukemia diagnosis from peripheral blood by pure light scattering *Sci. Rep.* **7** 12666
[3] Lippeveld M, Knill C, Ladlow E, Fuller A and Peralta D 2019 Classification of human white blood cells using machine learning for stain-free imaging flow cytometry *Cytometry* A **97** 308–19
[4] Yakimov B P, Gogoleva M A, Semenov A N, Rodionov S A and Shirshin E A 2019 Label-free characterization of white blood cells using fluorescence lifetime imaging and flow-cytometry: molecular heterogeneity and erythrophagocytosis *Biomed. Opt. Express* **10** 4220
[5] Schmit T, Klomp M and Khan M N 2021 An overview of flow cytometry: its principles and applications in allergic disease research *Methods Mol. Biol.* **2223** 169–82
[6] Liu S, Yuan Z, Qiao X, Liu Q and Su X 2021 Light scattering pattern specific convolutional network static cytometry for label-free classification of cervical cells *Cytometry* A **99** 610–21
[7] Sheng Y A and Dan Y B 2020 Continuous microfluidic 3D focusing enabling microflow cytometry for single-cell analysis *Talanta* **221** 121401
[8] Zhu S, Zhang X, Zhou Z, Han Y, Xiang N and Ni Z 2021 Microfluidic impedance cytometry for single-cell sensing: review on electrode configurations *Talanta* **233** 122571
[9] Song H *et al* 2013 A microfluidic impedance flow cytometer for identification of differentiation state of stem cells *Lab Chip* **13** 2300–10
[10] Zhou Y, Basu S, Laue E and Seshia A A 2016 Single cell studies of mouse embryonic stem cell (mESC) differentiation by electrical impedance measurements in a microfluidic device *Biosens. Bioelectron.* **81** 249–58
[11] Zhang Z, Zheng T and Zhu R 2020 Microchip with single-cell impedance measurements for monitoring osteogenic differentiation of mesenchymal stem cells under electrical stimulation *Anal. Chem.* **92** 12579–87
[12] Lei K F, Ho Y C, Huang C H, Huang C H and Pai P C 2021 Characterization of stem cell-like property in cancer cells based on single-cell impedance measurement in a microfluidic platform *Talanta* **229** 122259
[13] Marte B 2013 Tumour heterogeneity *Nature* **501** 327
[14] Dennis P 2011 Advances in hematology analyzers *Top. Companion Anim. Med.* **26** 52–61
[15] Chabot-Richards D S and George T I 2015 White blood cell counts: reference methodology *Clin. Lab. Med.* **35** 11–24
[16] Green R and Wachsmann-Hogiu S 2015 Development, history, and future of automated cell counters *Clin. Lab. Med.* **35** 1–10
[17] Choi H, Kim K B, Jeon C S, Hwang I, Lee S, Kim H K, Kim H C and Chung T D 2013 A label-free DC impedance-based microcytometer for circulating rare cancer cell counting *Lab Chip* **13** 970–7
[18] Rho J, Jang W, Hwang I, Lee D, Lee C H and Chung T D 2017 Multiplex immunoassays using virus-tethered gold microspheres by DC impedance-based flow cytometry *Biosens. Bioelectron.* **102** 121–8
[19] Song Y, Zhang J and Li D 2017 Microfluidic and nanofluidic resistive pulse sensing: a review *Micromachines* **8** 204
[20] Carey T R, Cotner K L, Li B and Sohn L L 2019 Developments in label-free microfluidic methods for single-cell analysis and sorting *Wiley Interdiscip. Rev. Nanomed. Nanobiotechnol.* **11** e1529
[21] Bausch C S, Heyn C, Hansen W, Wolf I, Diercks B-P, Guse A H and Blick R H 2017 Ultra-fast cell counters based on microtubular waveguides *Sci. Rep.* **7** 41584
[22] Mckinnon K M 2018 Flow cytometry: an overview *Curr. Protocols Immunol.* **120** 5.1.1–11
[23] Novo D, Ghosh K and Burke S 2018 Single cell and population level analysis of HCA data *Methods Mol. Biol.* **1683** 245–66
[24] Stavrakis S, Holzner G, Choo J and deMello A 2019 High-throughput microfluidic imaging flow cytometry *Curr. Opin. Biotechnol.* **55** 36–43
[25] Rožanc R J, Finšgar M and Maver U 2021 Progressive use of multispectral imaging flow cytometry in various research areas *Analyst* **146** 4985–5007
[26] Holmes D, She J K, Roach P L and Morgan H 2007 Bead-based immunoassays using a micro-chip flow cytometer *Lab Chip* **7** 1048–56
[27] Holmes D, Pettigrew D, Reccius C H, Gwyer J D, van Berkel C, Holloway J, Davies D E and Morgan H 2009 Leukocyte analysis and differentiation using high speed microfluidic single cell impedance cytometry *Lab Chip* **9** 2881–9
[28] Holmes D and Morgan H 2010 Single cell impedance cytometry for identification and counting of CD4 T-cells in human blood using impedance labels *Anal. Chem.* **82** 1455–61
[29] Barat D, Spencer D, Benazzi G, Mowlem M C and Morgan H 2012 Simultaneous high speed optical and impedance analysis of single particles with a microfluidic cytometer *Lab Chip* **12** 118–26
[30] Spencer D, Elliott G and Morgan H 2014 A sheath-less combined optical and impedance micro-cytometer *Lab Chip* **14** 3064–73
[31] Zhang Y, Liang H, Tan H, Chen D, Wang J and Chen J 2020 Development of microfluidic platform to high-throughput quantify single-cell intrinsic bioelectrical markers of tumor cell lines, subtypes and patient tumor cells *Sens. Actuators* B **317** 128231
[32] Zhao Y *et al* 2013 A microfluidic system enabling continuous characterization of single-cell specific membrane capacitance and cytoplasm conductivity *Biosens. Bioelectron.* **43** 304–7

[33] Zhao Y, Wang K, Chen D, Fan B, Xu Y, Ye Y, Wang J, Chen J and Huang C 2018 Development of microfluidic impedance cytometry enabling the quantification of specific membrane capacitance and cytoplasm conductivity from 100,000 single cells *Biosens. Bioelectron.* **111** 138–43

[34] Yang Z *et al* 2016 Electrical property characterization of neural stem cells in differentiation *PLoS One* **11** e0158044

[35] Wang K *et al* 2017 Membrane capacitance of thousands of single white blood cells *J. R. Soc. Interface* **14** 20170717

[36] Liang H, Tan H, Chen D, Wang J, Chen J and Wu M-H 2019 Single-cell impedance flow cytometry *Handbook of Single Cell Technologies* ed T S Santra and F-G Tseng (Berlin: Springer) pp 1–31